How do we evaluate the contribution of anthropogenic climate change to sea level rise from Antarctica?

Authors: Alexander T. Bradley[1,2], David T. Bett[1], Paul R. Holland[1], C. Rosie Williams[1], Robert Arthern[1], and Jan De Rydt[3]

[1]British Antarctic Survey, Cambridge, UK
[2]University of Cambridge, Cambridge, UK
[3]Northumbria University, Newcastle, UK

Corresponding author: Alexander T. Bradley (aleey@bas.ac.uk)

Note: This paper is a non-peer reviewed preprint submitted to EarthArXiv. It has been submitted to Nature Communications Earth and Environment for peer-review.

How do we evaluate the contribution of anthropogenic climate change to sea level rise from Antarctica?

Alexander T. Bradley*[1,2], David T. Bett[1], Paul R. Holland[1], C. Rosie Williams[1], Robert Arthern[1], and Jan De Rydt[3]

[1]British Antarctic Survey, Cambridge, United Kingdom

[2]Cambridge Zero, University of Cambridge, Cambridge, United Kingdom

[3]Department of Geography and Environmental Sciences, Northumbria University, Newcastle upon Tyne, UK

June 18, 2023

Abstract

The relative contributions of anthropogenic climate change and internal variability in sea level rise from the West Antarctic Ice Sheet are yet to be determined. Even the framework required to address this question is not yet clear, since these two are linked through ice-ocean feedbacks and probed using models with substantial structural uncertainty. Here, via a synthetic marine ice-sheet example, we demonstrate how their relative contributions can be assessed. Using a Bayesian approach, we construct distributions of sea level rise (SLR), accounting for uncertainties arising from both poorly-constrained model parameters and stochastic variations in climatic forcing, and demonstrate that it is necessary to account for both. We identify characteristic effects of climate change on SLR distributions, most notably that climate change increases both the median and the weight in tails of distributions. From these findings, we construct metrics quantifying the role of climate change, demonstrating that robust attribution of SLR is possible even for unstable marine ice sheets. This paves the way for real-world attribution studies, which have significant implications for climate damage reparations and greenhouse-gas emissions policy.

---

*aleey@bas.ac.uk

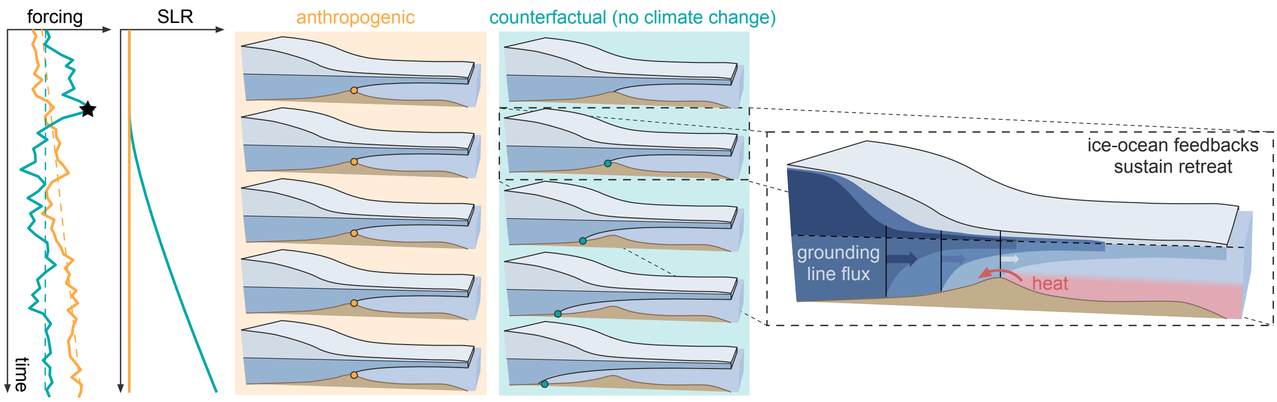

Fig. 1: Sea level rise from marine ice sheets is not necessarily an indicator of climate change. Schematic diagram demonstrating how an ice sheet configuration that remains stable under a realization of forcing including anthropogenic climate change (orange) may experience runaway retreat under a different, counterfactual realization of forcing with no anthropogenic climate change (green). As a result, grounding line retreat (filled dots in ice shelf configurations) and sea level rise are much higher in the counterfactual case. Once initiated (say, at the star), retreat from a topographic high is sustained by ice-ocean feedbacks.

Introduction

The West Antarctic Ice Sheet (WAIS) has changed significantly over the satellite era, characterized by ice acceleration [1], thinning [2], retreat [3], and ice loss [4]. The WAIS currently contributes approximately 10% of global SLR [5, 6] and could add tens of centimeters over the coming decades, possibly dominating by the end of the century [7]. However, despite being key symbols of anthropogenic climate change [8, 9], Antarctic ice loss, and thus associated sea level rise contributions, are yet to be formally attributed to anthropogenic climate change [10].

A robust causal relationship between WAIS ice loss and anthropogenic climate change is yet to be established because of strong internal variability in the region's climate and ice-ocean feedbacks which perpetuate ice loss [10]. There are several lines of evidence highlighting their complex interplay. While WAIS retreat was initiated in the 1940s [11–13], after an approximately 10,000-year quiescent period [14], anthropogenic influence on key climatological drivers in the region only became significant in the 1960s [15]. This suggests that the 'trigger' for retreat would have occurred even without anthropogenic forcing. Following its initiation, WAIS retreat was likely sustained by ice-ocean feedbacks [16–21] (figure 1). Most notably, retreat of this marine ice sheet across a retrograde bed (upward sloping in the flow direction) is associated with increased ice flux across the grounding line (where the ice transitions from sitting on bedrock to a floating ice shelf), which promotes further retreat [22, 23] (figure 1). Thus, one possibility is that the ongoing ice loss was triggered naturally in the 1940s and retreat is dominated by self-perpetuating feedbacks, playing out on the long timescales on which ice-sheets evolve [11, 13, 15, 24]. However, this retreat cannot be purely self-sustaining, independent of external forcing, because ice discharge remains responsive to ocean variability [25–27]. This picture is further complicated by a proposed centennial scale warming of the Amundsen Sea [24, 28], which is partly attributed to anthropogenic changes in large-scale climate systems [15, 28–30]. While all of these processes may contribute to the ongoing ice loss, the relative contributions of a historical trigger, ice-ocean feedbacks, and changes in climatic forcing are still unknown.

Determining the role of anthropogenic climate change in SLR from the WAIS is important for providing causal evidence to support recourse for the myriad social [e.g. 31], economic [e.g. 32], and ecological [e.g. 33] impacts of SLR, which are borne primarily by poorer and low-lying island nations [34]. This is particularly pertinent in light of the recent outcomes of the COP27 conference, in which a 'loss and damage' fund was established to compensate countries for the harm inflicted by anthropogenic climate change. In addition, attribution (or lack thereof) has implications for the future of the WAIS: if the observed ice loss is due solely to internal variability and ice-ocean feedbacks, sea level rise is likely already committed and irreversible; whereas, a significant anthropogenic component might suggest that ongoing contributions strongly depend on future greenhouse gas emissions.

Despite the importance of this question, a framework (i.e. an outline of the necessary experiments and analysis) to address it is not yet clear. Progress has been made towards such by Christian et al. [35], who considered how ice sheet retreat from a local topographic high under variable forcing may be attributed, using a one dimensional ice sheet model. Using a set retreat threshold as the 'event' to be detected, they showed that while an observation of significant retreat under a single realization of climatic forcing does not necessarily indicate that anthropogenic climate change was present in the forcing (figure 1), even modest anthropogenic trends in forcing make retreat more likely when averaged over multiple realizations. They conclude that a probabilistic approach, with multiple realizations of forcing, must be taken if robust attribution statements are to be made. Additionally, they showed that model parameter choices have a large impact on the likelihood of retreat, and thus the attribution statement; this suggests that multiple model parameters should be considered simultaneously in the attribution assessment, particularly when these are poorly constrained. Here, we present a framework for attributing sea level rise contributions from the WAIS which uses a probabilistic approach integrating multiple realizations of forcing; we build upon [35] by, firstly, explicitly accounting for the role of poorly-constrained model parameters in the attribution assessment and, secondly, considering sea level rise contributions, rather than retreat, as the metric to be attributed. Both of these advances emerge from our use of a Bayesian framework, which, in particular, allows an attribution metric to be constructed for any observed sea level rise, avoiding the need to specify a single 'event' that is to be attributed at the outset. We demonstrate this framework via an example of a marine-terminating ice sheet, which is highly susceptible to ice-ocean feedbacks and subject to forcing with strong internal variability, the characteristic features that are thought to obscure signals of anthropogenic climate change in SLR contributions from the WAIS. We explicitly construct distributions of SLR which simultaneously account for parametric uncertainty (that arising from poorly constrained model parameters) and aleatory uncertainty (that arising from an ice sheet's variable response to different realizations of stochastic forcing). We demonstrate their intimate interplay, as well as the necessity of considering both in WAIS ice loss projections, a feature that is lacking in current assumed estimates of sea level rise. These distributions also reveal characteristic signatures of anthropogenic forcing on distributions of SLR from marine ice sheets.

Results

Aleatory and parametric uncertainty in distributions of sea level rise

We adopt a Bayesian approach in which parametric uncertainty and aleatory uncertainty are simultaneously accounted for. As is standard, parametric uncertainty is accounted for by performing multiple simulations with different model parameters spanning the parameter space (for each realization of forcing), with the resulting SLR contributions weighted according to the level of agreement between a simulated and observed quantity [e.g. 36–40]. It is straightforward to incorporate aleatory uncertainty into such an approach (see methods) by placing no preference on the specific realization of forcing. Although accounting for parametric uncertainty in this way is now standard, no study has yet combined parametric and aleatory uncertainty, primarily because of the computational expense of doing so [38] (multiple simulations with different model parameters must be run for each additional realization of forcing).

To illustrate the approach, we focus on parametric uncertainty arising from the use of a parametrisation of ice shelf basal melting. Parameterisations of basal melting are often used instead of coupled-ice ocean models to reduce computational expense (in coupled ice-ocean models, the ocean component typically represents the vast majority of the expense [41]). Coupled ice-ocean models remain computationally intractable for the large ensembles of simulations [41] required to account for both aleatory and parametric uncertainty. However, parameterisations of melting neglect processes that have been shown to be important in determining basal melting [16, 42, 43], and simulations employing parameterisations have been shown to yield basal melt rates which result in poor skill at reproducing observed grounding line retreat [44] and ice loss [45–47], compared to coupled ice-ocean models. Our approach is intermediary: we use a parameterisation of basal melting to achieve computational efficiency and adopt a Bayesian approach to the model parameters within: simulations are weighted by comparing their predictions of basal melt rates with those from an offline ocean model at different snapshot times throughout a simulation (methods); the ocean model thus plays a role analogous to a ground-truth observation. We employ a common parameterisation of melting with quadratic dependence of melting on ocean temperature, in which a single dimensionless parameter M (effectively a calibration coefficient) is varied (methods).

Our example configuration features a prominent seabed ridge (figure 2a) on which the ice shelf is stably grounded (figure 2b) during an initialization stage with temporally constant ocean forcing, corresponding to typical conditions in the Amundsen Sea offshore of the WAIS (methods). This grounding line position, located at a topographic high, is reminiscent of the WAIS prior to the 1940s [11] and renders the system highly sensitive to ice-ocean feedbacks once grounding line retreat has been initiated [46]. We consider evolution from this steady state under variable ocean forcing, which is imposed by varying the depth of the pycnocline in the ambient ocean conditions (figure 2c–d). This forcing includes a stochastic internal variability component, which mimics the observed amplitude [48, 49] and persistence [35] of internal variability in ocean conditions in the Amundsen Sea on decadal and shorter timescales. Superimposed on this forcing is either an anthropogenic trend – a 100 m/century linear shallowing of the pycnocline, illustrating a plausible historical anthropogenically

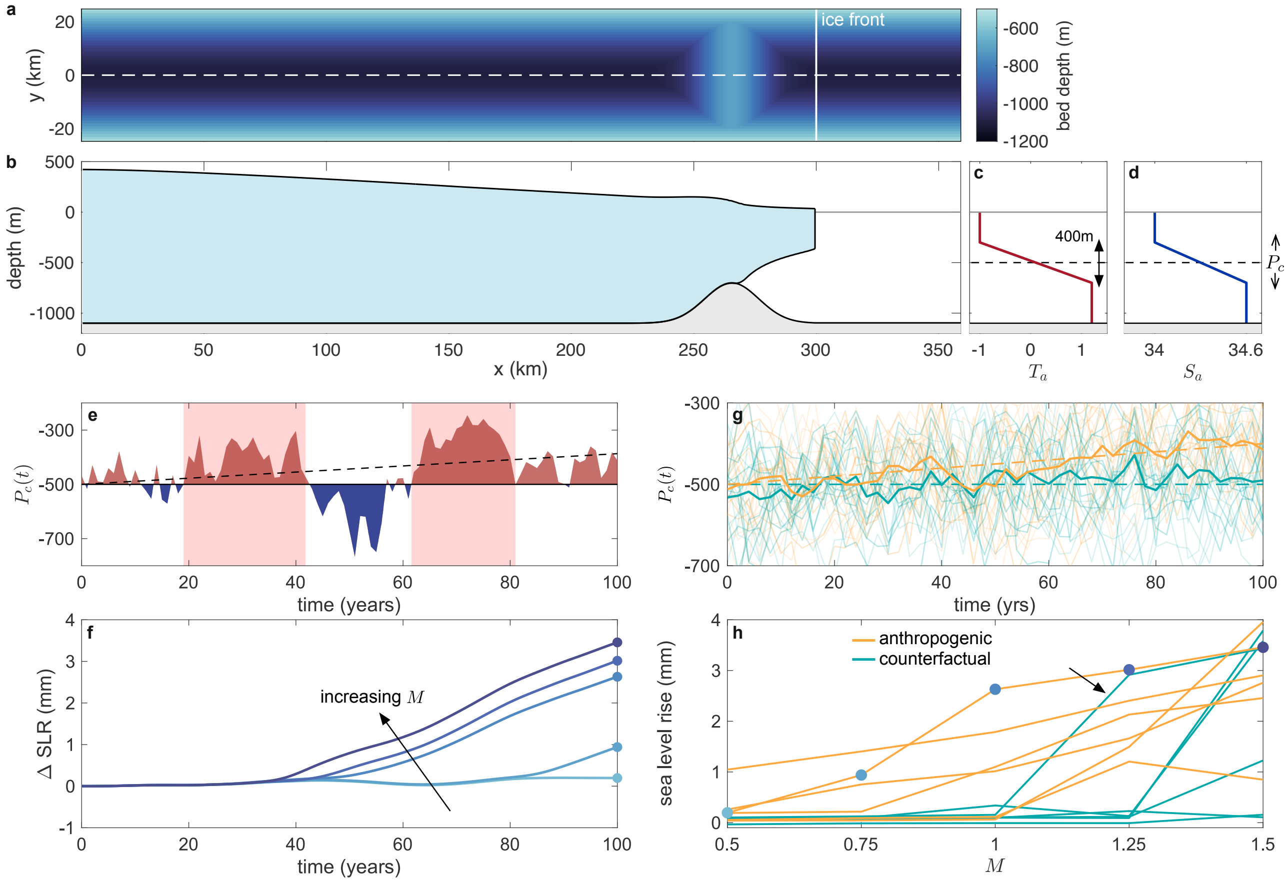

Fig. 2: Strong dependence of simulated marine ice sheet sea level rise on both forcing and model parameters. (a) Bathymetry (given by equation 7) of the marine ice sheet configuration. (b) Initial ice thickness along the dashed centerline in (a) for $M = 1$. The gray line indicates sea level. (c)–(d) Ambient temperature T_a (c) and salinity S_a (d) used in the parameterisation of melting and as restoring boundary conditions in the ocean model (methods). P_c denotes the pycnocline center, which parameterizes the piecewise linear forcing profiles and is oscillated to mimic variability. (e) Time evolution of a single realization of forcing and (f) corresponding SLR contributions for different values of $M \in \{0.5, 0.75, 1.0, 1.25, 1.5\}$ (the arrow indicates the direction of increasing M). Blue and red regions in (e) indicate whether the forcing is warmer (shallower pycnocline) or colder (deeper pycnocline) than during the calibration phase, where $P_c =$ -500 m (black horizontal line), and shaded red regions indicate two prominent warm periods. The black dashed line indicates the 100 m/century anthropogenic trend in the pycnocline depth. (g) Time evolution of pycnocline centres P_c in all realizations of forcing. Here, orange curves correspond to forcing scenarios with an anthropogenic trend of a 100 m/century shallowing of the pycnocline, while green curves correspond to a counterfactual scenario, with no trend in the forcing (methods). In both cases, faint curves indicate individual ensemble members, while solid curves indicate ensemble means, and the dashed lines indicate the respective trends in these. (h) Sea level rise after 100 years as a function of M for a sub-set of the different realizations of forcing. Each line corresponds to an individual realization of forcing, and colors indicate whether the forcing is drawn from the anthropogenic (orange) or counterfactual (green) ensemble. Blue hue points correspond to the points shown in panel f. The arrow indicates the curve referred to as the 'highlighted' curve in the main text.

driven trend in Amundsen Sea conditions [28, 50] – or no trend, representing the counterfactual scenario in which no anthropogenic climate change has taken place (figure 2g). For both of these trends (referred to as anthropogenic and counterfactual, respectively), we perform simulations with 40 independent realizations of forcing (the realizations in each of the two ensembles are also independent).

For each realization of forcing, we perform simulations sampling the set of M parameter space values. Requiring that the ice shelf remains stably grounded at the ridge crest during the initialization phase, and retreats under forcing corresponding to the warmest observed conditions applied constantly, restricts us to considering the range $0.5 < M < 1.5$ (methods); we sample this range by taking $M \in \{0.5,\ 0.75,\ 1.0,\ 1.25, 1.5\}$. Thus, the total number of simulations is 400 (2 ensembles $\times$ 40 members $\times$ 5 M values).

Examining the response to a single illustrative realization of forcing (figure 2e), for different melt parameters M, highlights the interplay between stochastic forcing and parameter variability, elucidating the inextricable relationship between aleatory and parametric uncertainty. On the centennial scale, this realization of forcing features two warm periods (figure 2e). During the first warm period (approximately between $t = 20$ and $t = 40$ years), retreat is triggered in those simulations with the largest values of M ($M = 1,\ 1.25,\ 1.5$; figure 2f). This retreat is initiated towards the end of the first warm period (figure 2f), when the time-integrated melt anomaly has caused enough ice shelf thinning to reduce ice shelf buttressing to the level at which retreat is initiated. Accordingly, retreat is initiated soonest in the simulation with the largest melt parameter M (figure 2f), which has the highest melt rates and accumulates the time-integrated melt anomaly most rapidly. Once initiated, retreat proceeds at a rate approximately independent of forcing (figure 2f), suggesting that, once triggered, retreat is set primarily by ice-ocean feedbacks, although it remains weakly responsive to changes in forcing. Simulations with smaller M (lower melting) remain grounded at the ridge crest during the first warm period. Retreat is initiated in the $M = 0.75$ simulation during the second warm period, again towards the end of the period. A simulation with the same realization of forcing with the anthropogenic trend removed, and $M = 0.75$, does not retreat during this period (note that this simulation is outside the ensemble structure outlined above, for which anthropogenic and counterfactual ensembles are independent): the integrated melt anomaly required to initiate retreat is achieved more easily during a given time period if there is an anthropogenic trend in the forcing, than if not.

Under the same realization of forcing, SLR may be highly non-linear in M (figure 2h). For example, SLR contributions in the highlighted curve in figure 2h increase by 1800% (from 0.15 mm to 2.91 mm after 100 years) when the melt rate parameter is increased from $M = 1$ to $M = 1.25$. This strong sensitivity demonstrates the necessity of considering a range of parameter values in determining SLR contributions, particularly when the system is susceptible to ice-ocean feedbacks, or so-called 'tipping points' may be passed. Furthermore, there are simulations in the anthropogenic ensemble which yield lower SLR than simulations in the counterfactual ensemble (figure 2h), and this behavior is strongly influenced by the value of M. Thus, an observation of high SLR under a single realization of forcing is not necessarily an indicator of strong anthropogenic influence (figure 1). Taken together, these results – a strong sensitivity to the parameter M and to the specific realization of forcing – demonstrate that parametric and aleatory uncertainty must be simultaneously accounted for in SLR distributions, and thus any framework attempting to determine the role of anthropogenic trends in forcing in them.

The non-linearity of sea level rise in M also demonstrates how single-point calibration (where the set of model parameters are specified based on agreement with a single observation, say the total melt flux out of an ice shelf cavity) may be problematic. Such single-point calibrations are often applied when tuning melt rate parameterisations [e.g. 47, 51, 52]. In the example presented here, the mean melt rate at the start of the simulation (at the end of the initialization stage, which is performed separately for different values of M) is only weakly dependent on the melt rate parameter (supplementary figure 7d), owing to a feedback between melting and ice geometry (methods). As a result, a small change in the target calibration value would result in a small change in the selected value of M (supplementary figure 7d), but may ultimately result in a large change in the simulated SLR at the end of the simulation (figure 2h).

Influence of anthropogenic forcing on sea level rise probability distributions

Applying the melt rate calibration procedure (methods), yields, for each time in each simulation, a distribution of sea level rise associated with the particular realization of forcing applied (supplementary figure 8). Then, by marginalizing over the realizations of forcing (methods), we obtain calibrated probability distributions of SLR for both anthropogenic and counterfactual ensembles, at each time (figure 3a).

The time evolution of both ensembles display qualitatively similar behavior. The evolution of the distributions can be categorized into two temporal parts: 'tail emergence' and 'shift towards tails' (figure 3c). At early times, the distributions are symmetric (figure 3a), with low skewness (figure 3c) reflecting retreat having not been triggered in any simulations. As retreat begins to be triggered in individual simulations, the 'tail emergence' period begins: a tail emerges (skewness increases, figure 3c) – supported by increasing SLR contributions from those already retreating simulations – and kurtosis increases (figure 3d), indicating that the relative weight in the tails is reducing (kurtosis quantifies the proportion of weight placed in the tails, with low kurtosis corresponding to heavy tails). The timescale on which the tails emerge depends on the forcing (see below). Median sea level rise remains small in the tail emergence period (figure 3b).

As retreat is triggered in an increasing number of ensemble members, weight begins to shift to the tails; the 'shift towards tails' period begins when skewness and kurtosis reach a maximum (figure 3c–d). Beyond this maximum, weight moves towards the tails (kurtosis reduces, figure 3d) and, in response to this, the median increases (figure 3a), continuing to the end of the simulation. (The median is a more appropriate metric than the mean given the skewed data.) Both medians display a non-linear evolution, reflecting non-linear SLR contributions in individual simulations once retreat has been initiated. Although the precise details of the evolution of the distributions depends on both the system and the forcing (see below), we expect that this qualitative behavior is generic in marine ice sheets with tipping points under high variability stochastic forcing.

Despite these qualitative similarities between the anthropogenic and counterfactual distributions, there are clear quantitative differences, which highlight the importance of the anthropogenic trend in forcing. Firstly, the tail emerges sooner in the anthropogenic ensemble (figure 3c), because retreats are initiated sooner when a trend in forcing is imposed (supplementary figure 5). This is despite the anthropogenic additional forcing being zero at the start of the simulation (figure 2g), highlighting the role played by increases in forcing during the time period in which the destabilizing integrated melt anomaly is accumulating: if forcing did not change over this period (or, if the changes did not matter), the first retreats would take place at approximately the same time in both ensembles. This is consistent with [15], who suggest that the current retreat of WAIS was triggered naturally in the 1940s, but may have subsequently failed to recover due to increasing influence of anthropogenic forcing towards the start of the 1960s. Secondly, the maximum skewness is lower, and achieved sooner, in the anthropogenic case (figure 3c). In a given time period, retreat is triggered in a greater proportion of simulations in the anthropogenic ensemble than in the counterfactual ensemble (supplementary figure 5), resulting in probability distributions shifting more quickly towards the heavy-tailed regime. This difference in retreat rate triggering is because, as time proceeds, melt anomalies under anthropogenic forcing become increasingly large, so a shorter positive anomaly duration is required to initiate retreat (more specifically, with a linear anthropogenic trend, the melt anomaly scales with the square of time, which rapidly outweighs any time-integrated negative internal component). Finally, and most importantly, on the centennial timescale, both the median is larger, and the kurtosis smaller, in the anthropogenic ensemble than in the counterfactual ensemble; i.e. not only does anthropogenic forcing increase the median of the distribution, it also results in greater weight in the tails: extreme events, with high sea level rise contributions, have relatively large probabilities in the anthropogenic ensemble. This emphasizes the need to consider the shape, as well as the spread (i.e. the variance), when communicating how emissions pathways affect future SLR scenarios with policymakers.

Figures 3b-d also indicate how summary statistics differ between the calibrated and uncalibrated distributions, with the latter obtained by setting the posterior probability equal to the prior probability (methods). In both ensembles, parametric calibration of M has an important effect on the median, evidencing the need to apply parametric calibration in projections of SLR from ice sheets. Reduced uncertainty in projections is often (perhaps implicitly) cited as a key benefit of parametric calibration [e.g. 36, 38]; whilst our simulations provide evidence to support this, displaying increased kurtosis (reduced weight in the tails; figure 3d) in the calibrated case, there remain significant uncertainties in calibrated distributions (figure 3a). This suggests that aleatory uncertainty is an unavoidably large part of uncertainty in projections of SLR from ice sheets, particularly those highly susceptible to ice-ocean feedbacks, and cannot be neglected: parametric calibration alone is not sufficient, and there is irreducible uncertainty in SLR from marine ice sheets.

Quantifying signals of anthropogenic climate change

The role of anthropogenic climate change in individual ‘weather’ events is often framed as an anthropogenic enhancement [53]: how many times more (or less) likely was the event made by anthropogenic climate change? Having constructed distributions of SLR in both anthropogenic and counterfactual cases, the ratio of these – the anthropogenic enhancement ratio (AER) – naturally emerges as a metric to quantify how many times more

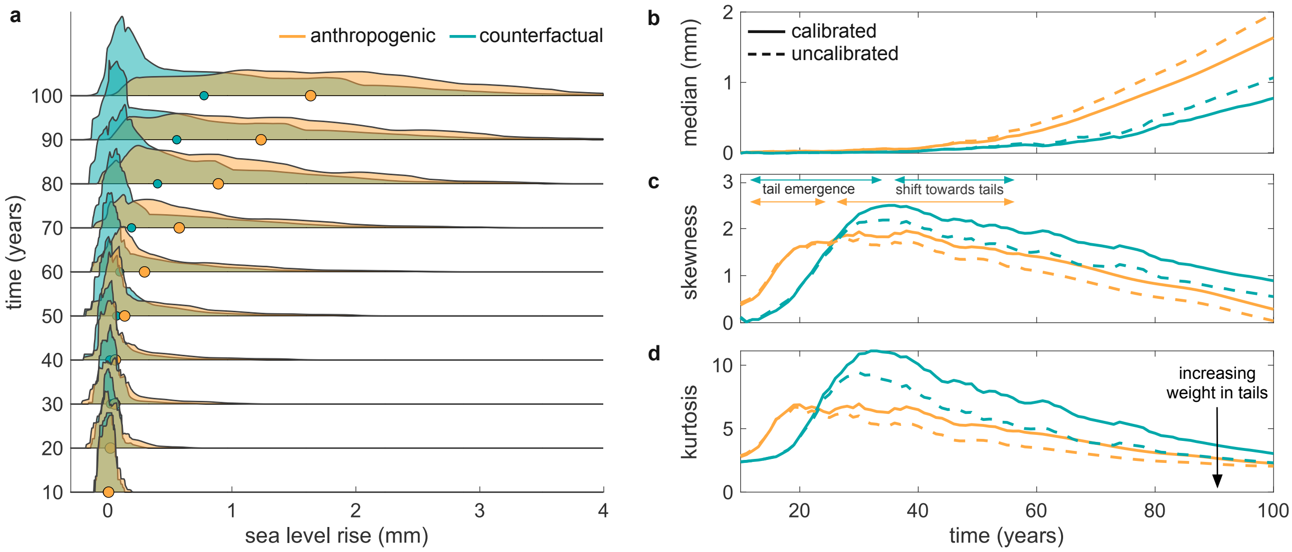

Fig. 3: Influence of anthropogenic forcing on distributions of sea level rise. (a) Time evolution (running bottom to top) of distributions of sea level rise from ensembles with anthropogenic forcing (orange) and counterfactual (no-trend) forcing (green). Filled markers indicate the median of the distributions at the corresponding time. (b)–(d) Summary statistics of the distributions in (a) as follows: (b) median, (c) skewness and (d) kurtosis. In each, the dashed lines indicate the corresponding summary statistics for distributions obtained without parametric calibration, obtained by setting the posterior probability equal to the prior probability.

likely an observed sea level rise was made by the presence of an anthropogenic trend in forcing, and go beyond the qualitative comparisons of the previous section. An AER of 2, for example, indicates that anthropogenic forcing made a given SLR contribution 100% more likely (or, equivalently, twice as likely). The AER for our ensembles is shown in figure 4a, where values along each line of constant time represent the ratio between the two distributions (as shown for specific times in figure 3a).

There is a band in which the AER is infinite, which is caused by the tails of the anthropogenic distribution extending to higher SLR values than those in the counterfactual distribution (figure 4a). An observation of SLR in this band would have been impossible without anthropogenic climate change–no counterfactual simulations produce this value. The band spreads out in time from an area close to the origin (recall that the tail of the anthropogenic distribution emerges soon after the start of the simulation) at a rate that is set by the retreat of the individual simulation with the highest SLR.

The AER is generally increasing in SLR, indicating that a higher SLR over many realizations of forcing is a stronger indicator of anthropogenic climate change. This demonstrates the importance, and value, of accounting for aleatory uncertainty: under a single realization of forcing, higher SLR does not necessarily indicate a strong influence of anthropogenic climate change (figure 1), but, does when appropriately averaged over many realizations of forcing. This also highlights the shift from a binary yes-no question, to a probabilistic approach, that necessarily takes place when accounting for aleatory uncertainty [35]. The AER has a slightly banded structure (figure 4a), which results from the finite size of our ensembles (there are periods when relatively more retreats are initiated than the background trend, see figure 5). While we expect that the banding would disappear as the number of realizations of forcing goes to infinity, we note that increasing this number is particularly computationally expensive when accounting for aleatory and parametric uncertainty simultaneously.

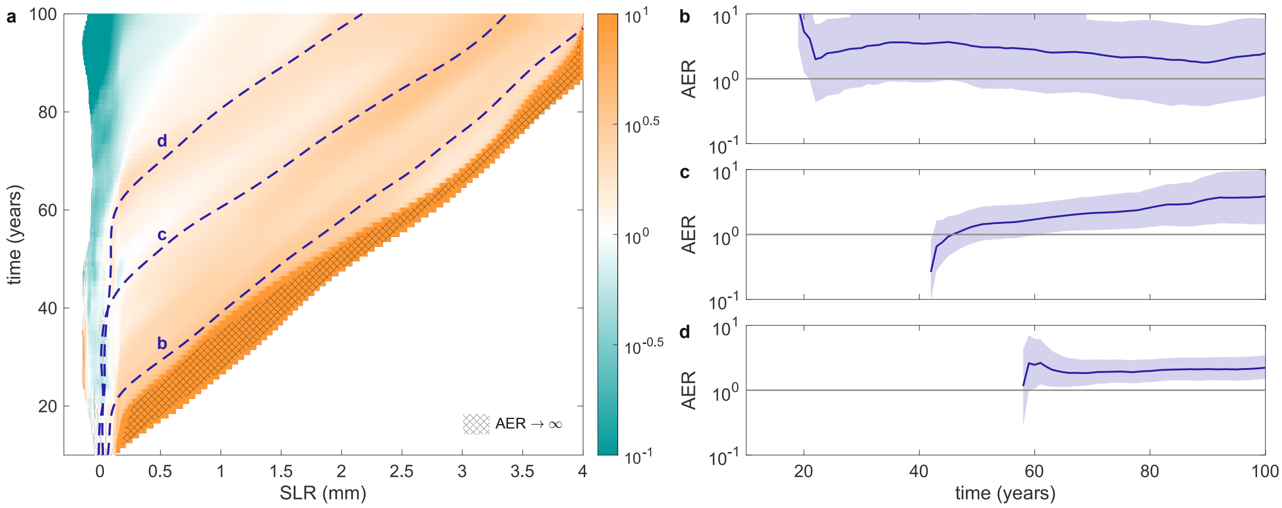

Fig. 4: Signals of anthropogenic climate change in sea level rise from marine ice sheets. (a) Contour plot of anthropogenic enhancement ratio (AER) as a function of time and space, with colors as indicated by the colorbar. The hatched region indicates the area where AER $\to \infty$. (b)–(d) Time evolution of AER (solid lines) along selected simulation trajectories of sea level rise, corresponding to labelled lines in (a). The shaded region indicates the uncertainty in this metric, obtained by bootstrapping values of distributions that result from individual realizations of forcing (methods). Data are shown only for times where SLR $>$ 0.1 mm for clarity.

In practice, observed sea level rise follows a single trajectory through this AER space, such as the selected simulations shown in figure 4b–d, in which retreat is triggered after approximately 20, 40, and 60 years, respectively (figure 4a). Their values are indicative of the clear signal of anthropogenic climate change: at the end of the simulation, AER is approximately 2.5, 3.9 and 2.2 respectively, corresponding to increases in probability of 150%, 290%, and 120%, respectively. These values are common along their paths, and once retreat has been triggered, the AER remains fairly constant. It is worth noting that these values are perhaps modest compared to glaciological attribution studies applied to mountain glaciers [e.g. 54, 55]. This is a direct consequence of our choice of setup: we consider a scenario in which internal variability is relatively large compared to the anthropogenic trend (and these selected trajectories don't enter the tail band, for which AER $\to \infty$).

From a policy perspective, a third useful question, beyond how to address and how to quantify the attribution question, is: what is the uncertainty in this quantification? Having constructed distributions associated with each realization of forcing (which the distributions shown in figure 3 are the mean over), such uncertainties can be probed. To do so, we bootstrap values of the distributions from individual realizations of forcing to determine a confidence interval (methods and supplementary figure 9) – a measure of the likely spread in AER – around our central estimates (figure 4b–d). Uncertainty in AER is generally smaller along contours corresponding to later retreat (figure 4b–d). This is commensurate with relatively few simulation trajectories entering the region in and around the tail band, leading to increased uncertainty: although the central estimate of anthropogenic enhancement is itself largest in the tails, there is most uncertainty in the value there. We expect that this error bound would reduce with increasing numbers of realizations of forcing. Thus, we expect that real world attribution studies will have to grapple with the limitation that increasing ensemble size is required to reduce uncertainty in the role of anthropogenic forcing, but requires substantial additional computational resource.

Discussion

The example presented here provides a probabilistic framework to assess the role of anthropogenic climate change in sea level rise contributions from the West Antarctic Ice Sheet, including both quantifying the strength of the anthropogenic signal and its uncertainty. Determining the precise influence of anthropogenic climate change on sea level rise contributions from the WAIS requires 'real-world' simulations to be performed. A key challenge to overcome will be determining an appropriate prior distribution for the historical state of the system: projections of ice sheet evolution are sensitive to their initial states, similar to numerical weather forecasts [56], but relatively little is known about the configuration of the WAIS prior to the satellite record beyond broad bounds on grounding line locations [11]. As such, it may be necessary to adopt semi-empirical approaches, such as expert elicitation [57], to construct such a prior. Our simplified example, with assumed knowledge of the initial state, circumvents this considerable difficulty, allowing the key interaction between parametric and aleatory uncertainty to be examined in detail.

In considering a generic marine ice sheet, we are also able to neglect uncertainty arising from model parameters governing basal sliding and ice viscosity, as well as processes such as damage [19, 58] and calving [43, 59, 60], which should be included in assessments of sea level rise and thus its attribution to anthropogenic climate change. By abstracting in this way, we are able to focus on errors in melting, with the hope that the melt calibration approach may help to bridge the considerable gap in fidelity to observations between parameterisations of melting and coupled ice-ocean simulations. It is important to note that additional parametric uncertainty, as well as uncertainties arising from incomplete knowledge of the initial state, can be succinctly assimilated into Bayesian approaches to sea level rise distributions [61]. The work presented can be considered, more generally, as a framework for producing calibrated distributions of sea level rise, in addition to their application to attribution statements. We have demonstrated that both aleatory and parametric uncertainty are important components of ice sheet sea level rise projections, and suggest that future assessments of sea level rise from ice sheets must account for these sources of uncertainty. As we have shown, parametric calibration reduces uncertainty, but the susceptibility to ice-ocean feedbacks renders broad distributions inevitable [62]: much like other aspects of the climate system [63], ice sheets have irreducible uncertainty. In addition, considering a range of initial states (which may be broad) will only increase this uncertainty. The glaciological community must become more comfortable with these fundamental aspects of uncertainty and appropriately communicate them to policy-makers and stakeholders.

By constructing calibrated distributions of sea level rise contributions, we showed that anthropogenic climate change increases both the median of distributions, and the relative weight of their tails: much like many other weather events [64], even modest anthropogenic climate change can make extreme scenarios many times more likely. Using these distributions, we constructed a metric to quantify the role of anthropogenic forcing, concluding that even in highly unstable marine ice sheets, the impact of anthropogenic forcing is detectable in principle, given sufficiently large simulation ensembles under anthropogenic and natural forcings and a full treatment of model parameter uncertainty. In other words, attribution studies are tractable for the WAIS.

The implications of attributing ice loss from the WAIS, both for the harms caused by sea level rise, and the implications for the future of the WAIS, provide strong motivation to pursue such studies.

Data Availability

Code to analyze data and produce figures herein is contained in an open GitHub repository at `https://github.com/alextbradley/WAISAttribution-figures`. Processed ice sheet and ocean model data is contained in a permanent Zenodo repository at `https://zenodo.org/record/7900762#.ZFUykOzMLPa`.

Methods

Sea level rise contributions accounting for parametric and aleatory uncertainty

For a given trend in forcing, denoted $\mathcal{F}$, (i.e. after specifying whether the trend is anthropogenic or counter-factual), the probability of a given SLR, ΔSLR, accounting for aleatory and parametric uncertainty may be expressed as [61]

$$P(\Delta\mathrm{SLR}|\mathcal{F},\mathcal{I}_0) = \frac{1}{n}\sum_{i=1}^{n}\int P(\Delta\mathrm{SLR}|\mathcal{F},\mathcal{N},\mathcal{R}_i,\mathcal{I}_0)P(\mathcal{N}|\mathcal{R}_i,\mathcal{F},\mathcal{I}_0)\ \mathrm{d}\mathcal{N}. \tag{1}$$

Here, $\mathcal{N}$ is the space of model parameters, n is the total number of realizations of forcing, R_i is the specific realization of forcing (with i a dummy index), and I_0 represents the initial conditions. The expression (1) follows from a first-principles probabilistic expression of SLR [61], after assuming that each specific realization of forcing has equal prior probability, $P(\mathcal{R}_i) = 1/n$, and that the initial state I_0 is known. For our specific application of (1), $\mathcal{N}$ is the space of melt rate parameters, $0.5 < M < 1.5$. Note that the expression (1) does not include any account of model structural uncertainty, which arises from the approximations that ice sheet models make, as well as their incomplete representation or omission of physical processes [61]. Such uncertainties can only be accurately probed by performing the same numerical experiments with an ensemble of different ice sheet models, typically in a model intercomparison exercise [e.g. 65] and is therefore beyond the scope of this work. (It should be noted that the WAVI ice sheet model used herein demonstrates good agreement with other state-of-the-art ice sheet models in the most recent ice sheet model intercomparison exercise [65].)

Melt Rate Calibration

The calibration of model parameters M enters distributions of SLR through the probability $P(M|\mathcal{R}_i,\mathcal{F},\mathcal{I}_0)$, which appears in (1) (here we use the specific parameter name M, rather than the generic name $\mathcal{N}$). Following a standard Bayesian approach, we assume a prior distribution on the parameters M (with hyperparameter μ), which is then updated as new information is assimilated through the likelihood. In our case, this assimilated information is melt rates from an offline ocean model (see below); denoting this information by $\mathcal{O}$, Bayes' rule states that

$$P(M|\mathcal{O},\mu) = \frac{P(\mathcal{O}|M,\mu)\ P(M|\mu)}{P(\mathcal{O}|\mu)} \tag{2}$$

The first term in the numerator on the right-hand side of (2) represents a likelihood function, describing how the prior distribution (second term in the numerator on the right-hand side) is updated to assimilate ocean model results. The prior distribution describes the state of belief in model parameters N prior to comparison with the ocean model. The left-hand side of (2) represents the posterior distribution – the distribution of parameters M following ocean model assimilation. The denominator of the right-hand side of (2) simply acts to normalize the probability distribution.

Here, we assume a Gaussian prior, which maximizes the relative entropy when only estimates of the prior mean μ and standard deviation σ_P are available [66, 67]:

$$P(M|\mu) = \frac{\alpha}{\sqrt{2\pi\sigma_P^2}} \exp\left(-\frac{|M-\mu|^2}{2\sigma_P^2}\right). \tag{3}$$

Here α is a normalization constant, which ensures that the distribution (3) integrates to unity when calibration bounds on M are imposed (see 'Ice Sheet Model Initialization' below). σ_P can be thought of as describing the strength of confidence in the initial estimate of M, which is centered about the hyperparameter μ: a low (high, respectively) σ_P corresponds to high (low) confidence that the hyperparameter μ represents the 'true' value of M. In the results contained herein, we use $\mu = 1.25$, based on agreement in the mean melt rate after the initialization stage (see 'Ice Sheet Model Initialization') but retain a broad prior ($\sigma_P = 0.2$, see supplementary figure 8), representing weak confidence in the prior distribution, which captures the relative insensitivity of mean melt rate on M during the initialization stage (see 'Ice Sheet Model Initialization').

To determine the likelihood $P(\mathcal{O}|M,\mu)$, we first specify calibration timeslices $\tau = \{\tau_1, \dots \tau_n\}$ and, for each timeslice, run the ocean model in the geometry set by the ice-only model. After doing so, we have two melt rate fields,

$$\dot{m}^k_{\text{param}} = \dot{m}_{\text{param}}(x, y, t = \tau_k|M), \tag{4}$$

$$\dot{m}^k_{\text{ocean-model}} = \dot{m}_{\text{ocean-model}}(x, y, t = \tau_k|M) \tag{5}$$

from the parameterisation of melting and from the ocean model, respectively, and for each timeslice $k = 1, \dots, n$. (Note that the ocean model depends on the melt rate parameter M via the ice-shelf cavity geometry.) A melt error functional D_j is determined by comparing these two fields. The particular choice of the form of the D_j is subjective, reflecting how melting should be penalized. Here, we take D_j to be the mean absolute error in the two melt fields on grid cells below 500 m depth. This reflects the fact that deep areas, typically close to grounding lines, have disproportionately large impacts on the dynamics of the grounded ice [68–70].

From the timeslice errors D_j, we determine an average error $D = (1/n)\sum_{j=1}^{n} D_i$. The likelihood is then determined from an exponential error model,

$$P(\mathcal{O}|M,\mu) = \frac{1}{\sqrt{2\pi\sigma_L^2}} \exp\left(-\frac{D^2}{2\sigma_L^2}\right). \tag{6}$$

Here σ_L is a melt error covariance, which describes how harshly errors in the melt rate from the parameterisation are penalized (with respect to the ocean model): for low σ_L, errors are penalized more harshly, whereas for high σ_L, errors are penalized less harshly. In the limit $\sigma_m \to \infty$, each parameter value M is assigned equal weight, and the posterior distribution is identical to the prior (supplementary figure 8). In the results presented here, we use $\sigma_L = 10$.

Details of end-member configuration

The setup of the generic marine ice sheet configuration is very similar to that of [46], who interrogated how ice-ocean feedbacks perpetuate retreat of an ice sheet from a seabed ridge using a coupled ice-ocean model under constant forcing scenarios. In this setup, the bathymetry (figure 2a) can be expressed as the sum of along-flow and cross-flow components:

$$B(x,y) = B_x(x) + B_y(y), \tag{7}$$

where

$$B_x(x) = 400 \exp\left[-\frac{\left(x - 265\times 10^3\right)}{2\sigma_b^2}\right] \text{ m}, \tag{8}$$

$$B_y(y) = -\left[500 + 600 \sin\left(\frac{\pi}{2} + \frac{\pi y}{5\times 10^4}\right)\right] \text{ m}. \tag{9}$$

Here, x and y are co-ordinates in the along- and cross-flow directions, respectively (the ridge is aligned along the cross-flow direction, see figure 2a). The cross-flow bathymetry contribution, $B_y(y)$, corresponds to a symmetric valley-like configuration, whose margins are located 500 m below sea level and whose center is 1100 m below sea level; the cross-flow bathymetry contribution, $B_x(x)$, corresponds to a Gaussian ridge with height 400 m and lengthscale $\sigma_b = 1.1\times 10^4$, which is superimposed on the valley at a position centered on $x = 265$ km.

Following [46], ice rheology is described by Glen's law with flow exponent $n = 3$. A constant rate factor $A = 2.94\times10^{-9}$ a^{-1} kPa^{-3} is applied everywhere, except for within 5 km of the ice margins (i.e. for $y < -20$ km and $y > 20$ km), where the rate factor is set to $A = 5.04\times 10^{-9}$ a^{-1} kPa^{-3}; this is to mimic the narrow, low viscosity, shear margins which are characteristic of WAIS outlet glaciers, particularly Pine Island Glacier [71]. The sliding coefficient is set to 20 m a $^{-1}$ kPa $^{-1}$ everywhere. Surface accumulation varies linearly from 15 m a^{-1} at the ice divide ($x = 0$ km) to 1 m a^{-1} at $x = 150$ km and is set to a constant value of 1 m a^{-1} between $x = 150$ km and the ice front ($x = 300$) km. The resulting total surface accumulation, 67.5 Gt a^{-1}, closely matches observations [72], while the spatial pattern respects reduced accumulation with reducing altitude.

WAVI Ice Sheet Model

Sea level rise contributions are determined from simulations using the Wavelet-based Adaptive-grid Vertically-integrated Ice-sheet model (WAVI) [67, 73], a finite volume ice sheet model including a treatment of both membrane and simplified vertical shear stresses [74]. WAVI uses a regular solution grid (here 1 km in both directions), which is refined dynamically during the solution procedure to facilitate solution speed and accuracy. The configuration contained herein is included in the WAVI documentation as an example (`https://rjarthern.github.io/WAVI.jl/`). WAVI assumes a fixed ice front position, which is set to $x = 300$ km (this is equivalent to prescribing a calving law that the calving flux is equal to the normal ice velocity at the ice front).

Melt rate parameterisation

Melting in the ice sheet model is parameterized according to a quadratic temperature law [75],

$$\dot{m} = M\Gamma\left(T_a - T_f\right)^2. \tag{10}$$

Here, M is a dimensionless melt rate parameter, which can be thought of as a calibration coefficient to be freely varied [47], T_a is the ambient temperature far from the ice shelf base (see below), T_f is the local freezing temperature and $\Gamma = 0.56$ m yr^{-1} °C^{-2} plays the role of an exchange coefficient between temperature and melt rate. (Using the nomenclature of [47, 76], $\Gamma = \gamma_T[\rho_w c_p/(\rho_i L)]^2$, where γ_T is an exchange velocity, ρ_w is water density, ρ_i is the ice density, c_p is the specific heat capacity of water, L is the latent heat of fusion). The formulation (10) essentially encodes two mechanisms which strongly affect ice shelf basal melting: (1) ice shelf melting is governed by the turbulent heat flux from the ocean to the ice, which varies like the product of ocean temperature and velocity; (2) ocean velocity increases with the local thermal forcing $(T_a - T_f)$ as meltwater is released, increasing the buoyancy forcing and thus circulation strength. This parameterisation has been used in numerous ice sheet modelling studies [see 41, and references therein], including the latest ISMIP assessments [76].

As is standard, we assume that the local freezing point depends linearly on pressure and salinity, $T_f = \lambda_1 S_a + \lambda_2 + \lambda_3 z_b$, where $\lambda_1 = -5.73 \times 10^{-2}$ °C is the liquidus salinity slope, $\lambda_2 = 8.32 \times 10^{-2}$ °C is the liquidus intercept, $\lambda_3 = 7.61 \times 10^{-4}$ °C m^{-1} is the liquidus depth slope, S_a the ambient salinity (see below), and z_b is the depth of the ice shelf base.

We take a layered structure for the ambient temperature and salinity (figure 2c–d), parameterized solely via the depth of the pycnocline centre, P_c (which is in general time-dependent), and the pycnocline half-width w:

$$T_a(z; P_c, w) = \begin{cases} 1.2 & z < P_c - w \\ 1.2 - 2.2\frac{z-(P_c-w)}{2w} & P_c - w \leq z \leq P_c + w \\ -1 & z > P_c + w \end{cases} \tag{11}$$

$$S_a(z; P_c, w) = \begin{cases} 34.6 & z < P_c - w \\ 34.6 - 0.6\frac{z-(P_c-w)}{2w} & P_c - w \leq z \leq P_c + w \\ 34.0 & z > P_c + w \end{cases} \tag{12}$$

The profiles (11) and (12) are piecewise linear functions of depth (figure 2b): they are constant in both an upper (temperature -1°C, salinity 34 PSU, corresponding to Winter Water) and lower layer (temperature 1.2 °C, salinity 34.6 PSU, corresponding to Circumpolar Deep Water), which are separated by a pycnocline of $2w$ m thickness, across which the temperature and salinity vary linearly. These piecewise linear profiles are approximations to typical conditions in the Amundsen Sea [26, 49]. Here, we take $w = 200$ m, corresponding to a pycnocline width of 400 m, which is consistent with observations. Time varying stochastic forcing is applied by varying the pycnocline center (see ‘Stochastic Forcing’ below).

MITgcm Ocean Model

Ocean model melt rates used as calibration data are calculated by resolving the ice shelf cavity circulation using the Massachusetts Institute of Technology General Circulation Model (MITgcm) [77]. The procedure applied to determine ocean model melt rates at timeslices $\tau_1, \ldots, \tau_n$ under a given forcing $P_c(t)$ is as follows: (1) run the ice sheet model (with parameterized melting) under this forcing profile; (2) use the output of this to determine ice shelf geometries at timeslices $t = \tau_1, \ldots, \tau_n$; (3) for each of these geometries, run the ocean model in this geometry, with forcing applied via a restoring boundary condition corresponding to the profiles $P_c(\tau_k)$. The restoring boundary condition is applied at the downstream end of the domain at $x = 360$ km (figure 2a), where the temperature and salinity are restored to vertical profiles T_a and S_a over a distance of five horizontal grid cells with a restoring timescale of 12 hours. An example of melt rates fields $\dot{m}^k_{\text{param}}$ and $\dot{m}^k_{\text{ocean-model}}$ produced by this procedure is shown in figure 6.

The ocean model grid has 55 layers with a vertical spacing of $\mathrm{d}z = 20$ m, and a horizontal resolution of $\mathrm{d}x = 1$ km. We use the MITgcm in hydrostatic mode with an implicit nonlinear free surface scheme, a third-order direct space-time flux limited advection scheme, and a non-linear equation of state [78]. The Pacanowski-Philander [79] scheme parameterizes vertical mixing. Constant values of 15 and 2.5 $\mathrm{m}^2\ \mathrm{s}^{-1}$ are used for the horizontal Laplacian viscosity and horizontal diffusivity, respectively. The equations are solved on an f-plane with $f = -1.4 \times 10^{-4}\ \mathrm{s}^{-1}$. For each geometry, the MITgcm is run for three months, using a timestep of 30 seconds, after which the configuration is in quasi-steady state. The ocean model melt rate is taken as the melt rate after three months of the simulation. The drag coefficient in the three-equation formulation of melting [80] used in the MITgcm is taken to be 9×10^{-3}; this value ensures that the ocean model melt rate in the post-initialization geometries (see ‘Ice Sheet Model Initialization’) closely matches observed total meltwater flux values [e.g. 49] from Pine Island Glacier.

Ice Sheet Model Initialization

Following [46], we apply a two-stage initialization procedure, outlined in figure 7a. In the first initialization stage, the ice geometry is timestepped from an initial configuration in which the ice-surface is 150 m above sea level for 50 years (note that WAVI uses a hydrostatic flotation condition, so specifying the ice surface and bed elevation prescribes the ice thickness everywhere). Following this, the ice is approximately in steady state, with ice shelf geometry shown in figure 7c.

In the second stage of the initialization procedure, melting is turned on (figure 7). The ice geometry is then timestepped from that at the end of the first initialization stage for fifty years using a constant ocean forcing with $P_c = -500$ m. This pycnocline depth corresponds to typical conditions offshore of the WAIS (i.e. neither warm not cold) [48, 49]. In the following, we refer to warm forcing as constant forcing with $P_c = -400$ m, corresponding approximately to the shallowest recorded pycnocline depth [48]. Similarly, we refer to cold forcing as constant forcing with $P_c = -600$ m, corresponding approximately to the deepest recorded pycnocline depth [48]. The second initialization stage is performed independently for each value of M. The (M-dependent) state at the end of the second initialization stage (figure 7c) is then used as the initial condition in the following retreat simulations (figure 7).

Note that for a consistent estimate of sea level rise contributions from simulations with different values of M, we require similar initial conditions, chosen to be a grounding line at or near the seabed ridge crest. For $M \gtrsim 1.5$, the ice retreats irreversibly down the ridge during the second initialization stage. We therefore consider only M values smaller than this. In addition, we should impose that a constant warm forcing applied to the shelf should initiate retreat (WAIS retreat was, in practice, hypothesised to be initiated with forcing oscillating between warm and cold [11]); we found that for $M \lesssim 0.5$, no ice sheet retreat was initiated under warm forcing. Therefore, we restrict ourselves to the range $0.5 \leq M \leq 1.5$. Note that this restriction is consistent with our Bayesian framework: it is equivalent to setting the prior density to zero outside the range $0.5 \leq M \leq 1.5$, based on observational constraints.

During the second initialization stage, the ice shelf thins in response to applied melting, but the grounding line does not retreat (figure 7c). The mean melt rate after the second initialization stage is only weakly dependent on M (figure 7b). If the geometries at the end of the second initialization were identical for different values of M, the mean melt rate in the simulation with $M = 1.5$ would be 3 times as large as that with $M = 0.5$ (black dashed line in figure 7b); however, owing to temperature-depth effects, this value is only approximately 1.1 times (approximately 23.5 m year^{-1} in the $M = 1.5$ case versus approximately 21.3 m year^{-1} in the $M = 0.5$ case, see figure 7b). As the ice shelf thins in response to melting, it shallows, exposing it to colder ocean conditions, reducing melt rates sharply and restricting further thinning (the melt rate is proportional to $(T_a - T_f)^2$, which varies sharply with depth, particularly in the depth range occupied by the ice shelf in the second calibration phase, see figure 7d).

Stochastic Forcing

Following the two stage initialization in outlined above, stochastic forcing is applied via ambient ocean conditions:

$$P_c(t, \mathcal{F}) = p_{c,0} + T(\mathcal{F}) + A\mathcal{R}(t) \tag{13}$$

where $P_{c,0} = -500$ m is the pycnocline depth in the second stage of the initialization procedure, $T(\mathcal{F})$ is a forcing-scenario-dependent (i.e. anthropogenic or counterfactual) trend (see below), A is the amplitude of random forcing, and $\mathcal{R}(t)$ is a first-order autoregressive process, containing the stochastic part of the forcing. In the results shown here, we use $A = 100$ m, which agrees with observed internal variability in the Amundsen Sea [49]. In a first-order autoregressive time-series, the following value is decomposed into a component proportional to the current entry, whose constant of proportionality describes the persistence timescale of the variability, and an additive white-noise term. We take the same autocorrelation function as [35], with yearly-to-interdecadal timescales represented.

Anthropogenic and counterfactual ensembles are distinguished via the trend $T(\mathcal{F})$: realizations of forcing from the counterfactual ensemble have no trend added to them, $T = 0$; realizations of forcing in the anthropogenic ensemble have a linear trend, $T = A_0(t/100 \text{ yrs})$, where $A_0 = 100$ m is the per-century shallowing trend of the pycnocline (figure 2g).

Bootstrapping distributions of sea level rise

Each of the n realizations of forcing yields a parametrically-calibrated distribution of sea level rise for each time in the simulation. Thus, for any time and any sea level rise, we have n values of the distributions from both anthropogenic and counterfactual ensembles (supplementary figure 9). An uncertainty estimate in the anthropogenic enhancement ratio is constructed by bootstrapping these values – resampling from these n values with replacement (here, we sample 1000 times); the resulting set yields a standard deviation $\lambda = \lambda(SLR, t)$ for both anthropogenic and counterfactual ensembles (supplementary figure 9). Using subscripts to denote the ensemble (that is, counterfactual or anthropogenic), the upper bound shown in figure 4b–d is then computed as

$$AER_{\text{upper}} = \frac{\ell_{\text{anthro}} + \lambda_{\text{anthro}}}{\ell_{\text{counter}} - \lambda_{\text{counter}}} \tag{14}$$

where $\ell = \ell(SLR, t)$ is the probability density. Similarly, the lower bound is computed as

$$AER_{\text{lower}} = \frac{\ell_{\text{anthro}} - \lambda_{\text{anthro}}}{\ell_{\text{counter}} + \lambda_{\text{counter}}}. \tag{15}$$

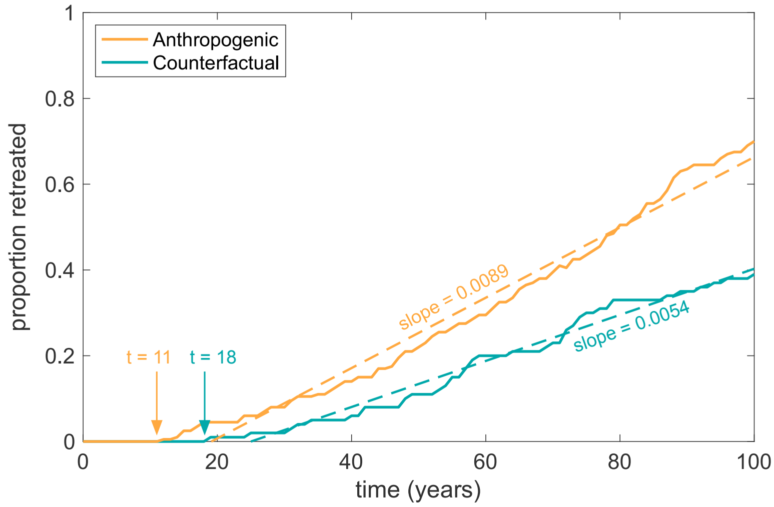

Fig. 5: Time evolution of retreats. Time evolution of the number of retreats (defined as a sea level rise contribution greater than 0.2 mm) for all simulations from the anthropogenic ensemble (yellow) and counterfactual (green). Arrows indicate the time at which the first retreat is initiated.

497 # Supplementary Figures

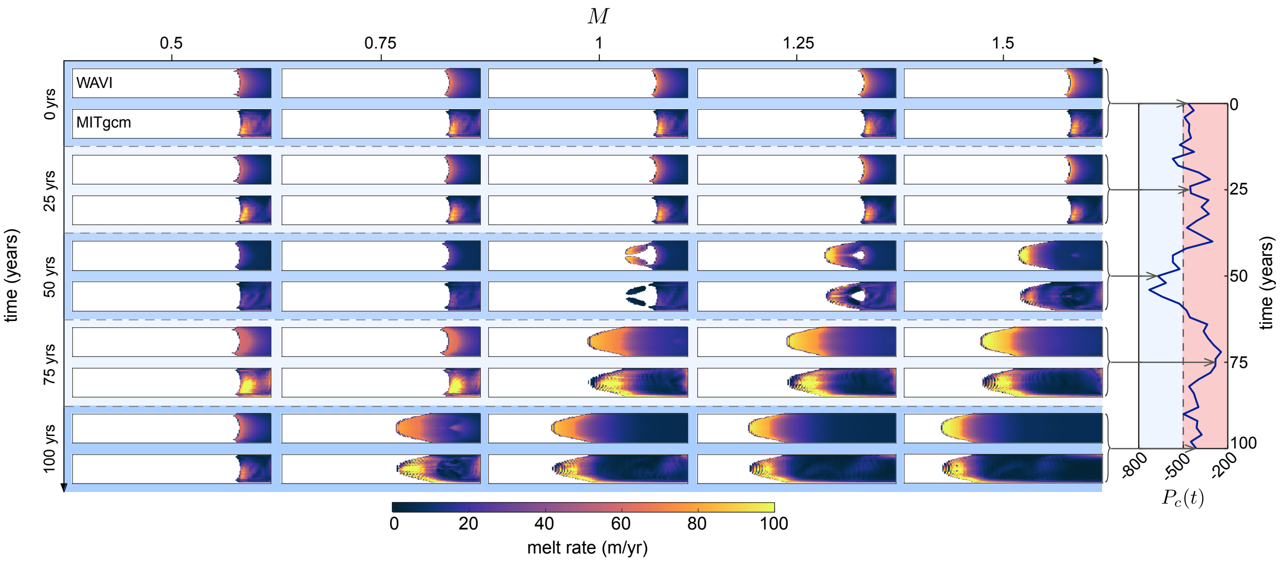

Fig. 6: Calibrated retreat of ice sheets under stochastic forcing. Ice shelf melt rates (colors) computed using parameterized melting in the WAVI ice sheet model (top of each sub-panel) and the MITgcm ocean model (bottom of each panel). Data are shown for different calibration timeslices (rows) and different melt rate parameter values M (columns). Note that the x- and y-axes are the same in each, and zoomed in on the ice shelf (100 km $< x <$ 300 km, -25 km$< y <$ 25 km). The side-panel indicates the realization of forcing corresponding to the main panel, showing pycnocline depth (abscissa) as a function of time (ordinate). Red (blue, respectively) indicates where the pycnocline is shallower (deeper) than its initial position, $P_c(0) = -500$ m.

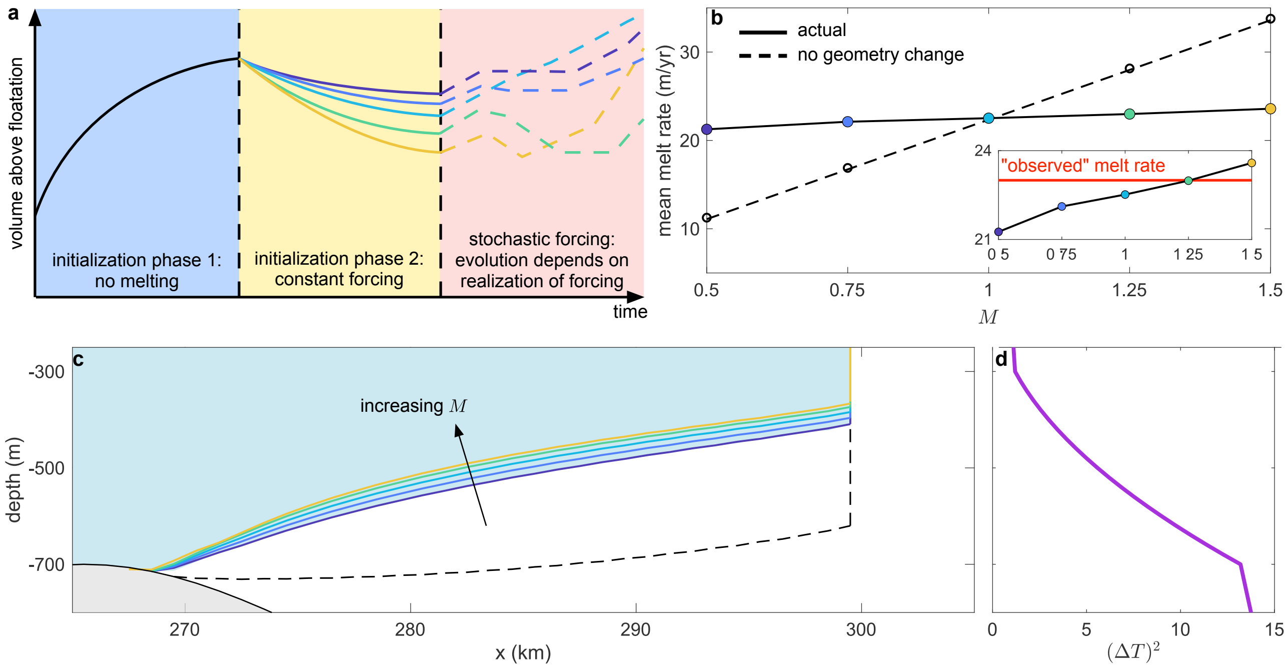

Fig. 7: Two stage initialization procedure. (a) Schematic diagram of the initialization procedure, described in 'Ice Sheet Model Initialization'. Colors in the second calibration phase correspond to different values of M, as indicated by points in (b). (b) Mean melt rate after the second calibration phase as a function of M (solid line). The dashed line indicates what the mean melt rate would be if the same geometry (that of the $M = 1$ case) were used for each value of M. Inset: as in main panel with a zoomed ordinate axis. The red line is the target calibration value of 23 m year^{-1}, which acts as an artificial observation. (c) Ice shelf geometry after the first (black) and second (colors, according to colors in (b)) initialization stages. (d) Squared thermal forcing $(\Delta T)^2 = (T_a - T_f)^2$ as a function of depth (note that (c) and (d) share an ordinate axis).

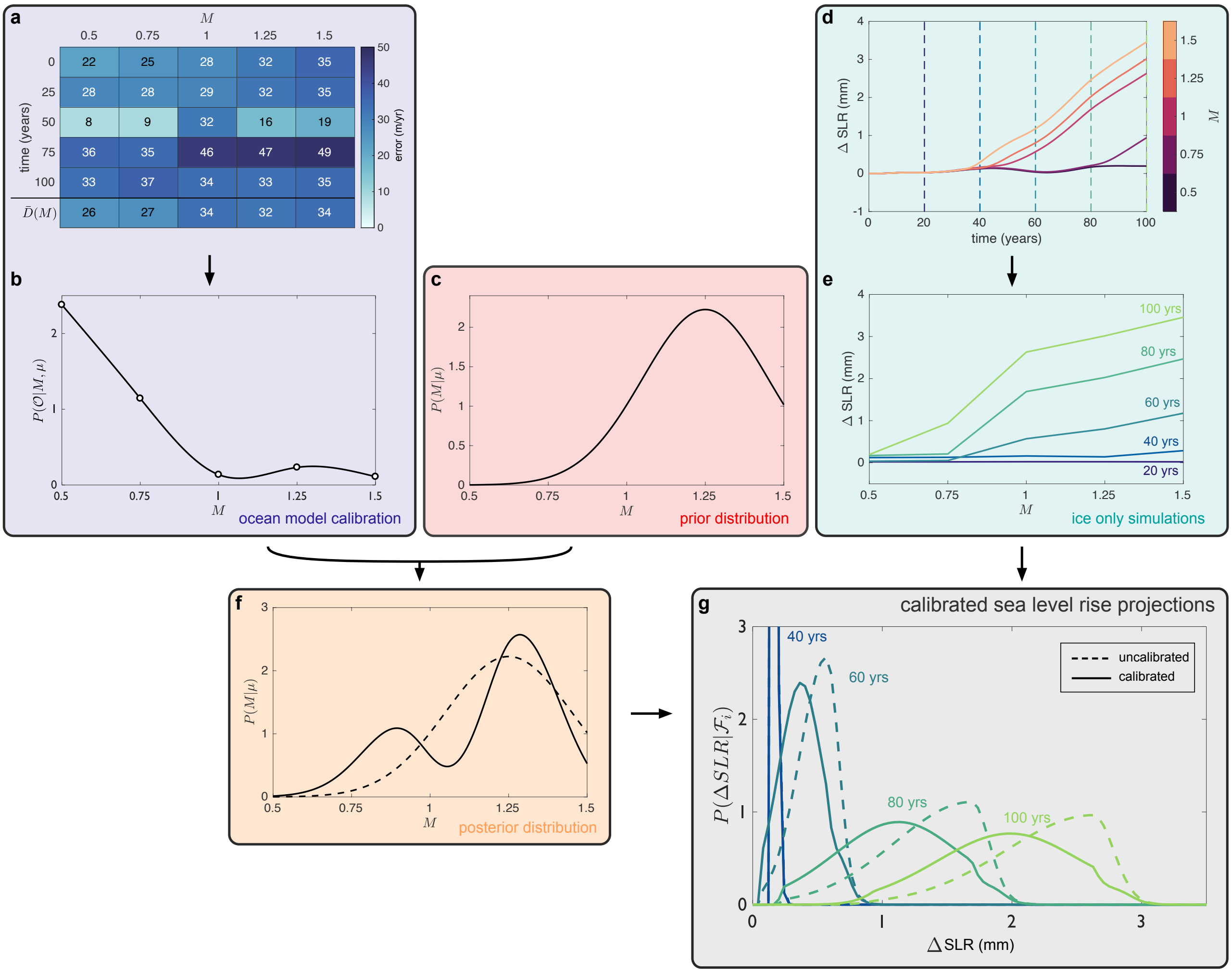

Fig. 8: Producing parametrically calibrated distributions for a given realization of forcing. (a) Likelihood values at each calibration timeslice (rows) as a function of M, for the realization of forcing shown in figure 2e and supplementary figure 6. Dark (light, respectively) colors indicate high (low) errors in melting. The final row indicates the discrepancy D as a function of M, computed as the mean over calibration timeslices. (b) Likelihood function $P(\mathcal{O}|M, \mu)$ (given by equation (6)), describing how the prior distribution is updated to account for information introduced by the ocean model. Here, $\sigma_L = 10$ m year^{-1}. (c) Prior distribution, given by equation (3), representing the state of knowledge of parameters M prior to calibration. Here, $\sigma_P = 0.2$. (d) Sea level rise as a function of time for different values of M (indicated by colors), for the realization of forcing shown in figure 2e. (e) Sea level rise at fixed times (indicated by colors, corresponding to dashed vertical lines in (d)) as a function of M. (f) Posterior distribution of M (solid black line), obtain by combining the prior and likelihood according to (2). The dashed black line shows the posterior distribution for M for reference. (g) Combining the posterior distribution with sea level rise data yields calibrated probability distributions, for the forcing profile shown in figure 2e. Data are shown for different times, as labelled.

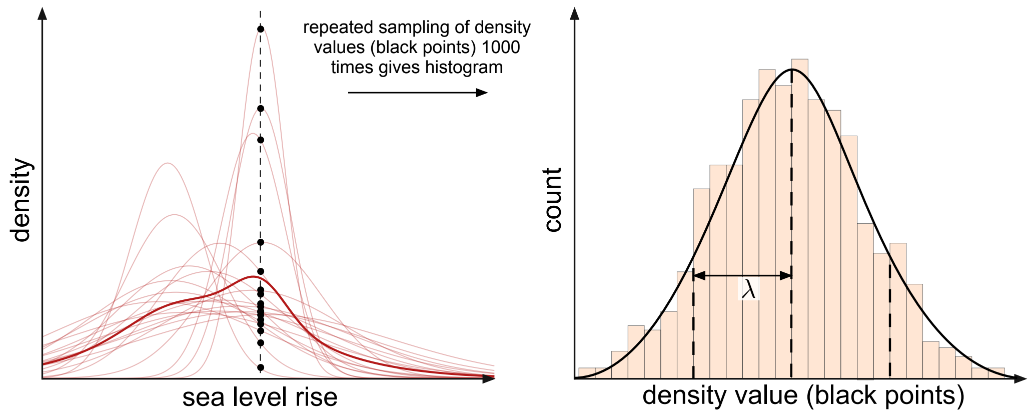

Fig. 9: Schematic diagram of the bootstrapping procedure. (left) For any given time, we obtain a unique distribution of sea level rise for each realization of forcing (faint lines), whose ensemble mean (solid line) is the central distribution after accounting for aleatory uncertainty. For a given sea level rise value, an estimate of the variance λ is determined by sampling the values of the individual PDFs 1000 times and taking the standard deviation of the resulting distribution (right).

References

1. Mouginot, J., Rignot, E. & Scheuchl, B. Sustained increase in ice discharge from the Amundsen Sea Embayment, West Antarctica, from 1973 to 2013. *Geophysical Research Letters* **41,** 1576–1584 (2014).
2. Smith, B. *et al.* Pervasive ice sheet mass loss reflects competing ocean and atmosphere processes. *Science* **368,** 1239–1242 (2020).
3. Rignot, E., Mouginot, J., Morlighem, M., Seroussi, H. & Scheuchl, B. Widespread, rapid grounding line retreat of Pine Island, Thwaites, Smith, and Kohler glaciers, West Antarctica, from 1992 to 2011. *Geophysical Research Letters* **41,** 3502–3509 (2014).
4. IMBIE. Mass balance of the Antarctic Ice Sheet from 1992 to 2017. *Nature* **558,** 219–222 (2018).
5. Otosaka, I. N. *et al.* Mass balance of the Greenland and Antarctic ice sheets from 1992 to 2020. *Earth System Science Data* **15,** 1597–1616 (2023).
6. Wouters, B., van de Wal, R., *et al.* Global sea-level budget 1993–present. *Earth System Science Data* **10,** 1551–1590 (2018).
7. Edwards, T. L. *et al.* Projected land ice contributions to twenty-first-century sea level rise. *Nature* **593,** 74–82 (2021).
8. Leiserowitz, A. Communicating the risks of global warming: American risk perceptions, affective images, and interpretive communities. *Creating a climate for change: Communicating climate change and facilitating social change,* 44–63 (2007).
9. Lehman, B., Thompson, J., Davis, S. & Carlson, J. M. Affective images of climate change. *Frontiers in psychology* **10,** 960 (2019).

10. Meredith, M. M. *et al.* Polar Regions. In: IPCC Special Report on the Ocean and Cryosphere in a Changing Climate [H.-O. Pörtner, D.C. Roberts, V. Masson-Delmotte, P. Zhai, M. Tignor, E. Poloczanska, K. Mintenbeck, A. Alegría, M. Nicolai, A. Okem, J. Petzold, B. Rama, N.M. Weyer (eds.)] (2019).

11. Smith, J. A. *et al.* Sub-ice-shelf sediments record history of twentieth-century retreat of Pine Island Glacier. *Nature* **541,** 77–80 (2017).

12. Steig, E. J., Ding, Q., Battisti, D. & Jenkins, A. Tropical forcing of Circumpolar Deep Water inflow and outlet glacier thinning in the Amundsen Sea Embayment, West Antarctica. *Annals of Glaciology* **53,** 19–28 (2012).

13. O'Connor, G. K., Holland, P. R., Steig, E. J., Dutrieux, P. & Hakim, G. J. Drivers and rarity of the strong 1940s westerly wind event over the Amundsen Sea, West Antarctica. *The Cryosphere Discussions* **2023,** 1–26 (2023).

14. Larter, R. D. *et al.* Reconstruction of changes in the Amundsen Sea and Bellingshausen sea sector of the West Antarctic ice sheet since the last glacial maximum. *Quaternary Science Reviews* **100,** 55–86 (2014).

15. Holland, P. R. *et al.* Anthropogenic and internal drivers of wind changes over the Amundsen Sea, West Antarctica, during the 20th and 21st centuries. *The Cryosphere* **16,** 5085–5105 (2022).

16. De Rydt, J., Holland, P. R., Dutrieux, P. & Jenkins, A. Geometric and oceanographic controls on melting beneath Pine Island Glacier. *J. Geophys. Res. Oceans* **119,** 2420–2438 (2014).

17. Favier, L. *et al.* Retreat of Pine Island Glacier controlled by marine ice-sheet instability. *Nature Climate Change* **4,** 117–121 (2014).

18. Bett, D. T. *et al.* The impact of the Amundsen Sea freshwater balance on ocean melting of the West Antarctic Ice Sheet. *Journal of Geophysical Research: Oceans* **125,** e2020JC016305 (2020).

19. Lhermitte, S. *et al.* Damage accelerates ice shelf instability and mass loss in Amundsen Sea Embayment. *Proceedings of the National Academy of Sciences* **117,** 24735–24741 (2020).

20. Bradley, A., Bett, D., Dutrieux, P., De Rydt, J. & Holland, P. The influence of Pine Island Ice Shelf calving on basal melting. *Journal of Geophysical Research: Oceans* **127,** e2022JC018621 (2022).

21. Holland, P. R., Bevan, S. L. & Luckman, A. J. Strong ocean melting feedback during the recent retreat of Thwaites Glacier. *Geophysical Research Letters* **50,** e2023GL103088 (2023).

22. Weertman, J. Stability of the junction of an ice sheet and an ice shelf. *Journal of Glaciology* **13,** 3–11 (1974).

23. Schoof, C. Ice sheet grounding line dynamics: Steady states, stability, and hysteresis. *Journal of Geophysical Research: Earth Surface* **112** (2007).

24. Holland, P. R., Bracegirdle, T. J., Dutrieux, P., Jenkins, A. & Steig, E. J. West Antarctic ice loss influenced by internal climate variability and anthropogenic forcing. *Nature Geoscience* **12,** 718–724 (2019).

25. Christianson, K. *et al.* Sensitivity of Pine Island Glacier to observed ocean forcing. *Geophysical Research Letters* **43,** 10–817 (2016).

26. Jenkins, A. *et al.* West Antarctic Ice Sheet retreat in the Amundsen Sea driven by decadal oceanic variability. *Nat. Geosci.* **11,** 733–738 (2018).

27. Christie, F. D., Steig, E. J., Gourmelen, N., Tett, S. F. & Bingham, R. G. Inter-decadal climate variability induces differential ice response along Pacific-facing West Antarctica. *Nature Communications* **14,** 93 (2023).

28. Naughten, K. A. *et al.* Simulated Twentieth-Century Ocean Warming in the Amundsen Sea, West Antarctica. *Geophysical Research Letters* **49,** e2021GL094566 (2022).

29. O'Connor, G. K., Steig, E. J. & Hakim, G. J. Strengthening Southern Hemisphere Westerlies and Amundsen Sea Low Deepening Over the 20th Century Revealed by Proxy-Data Assimilation. *Geophysical Research Letters* **48,** e2021GL095999 (2021).

30. Dalaiden, Q., Goosse, H., Rezsöhazy, J. & Thomas, E. R. Reconstructing atmospheric circulation and sea-ice extent in the West Antarctic over the past 200 years using data assimilation. *Climate Dynamics* **57,** 3479–3503 (2021).

31. Graham, S. *et al.* The social values at risk from sea-level rise. *Environmental Impact Assessment Review* **41,** 45–52 (2013).

32. Hinkel, J. *et al.* Coastal flood damage and adaptation costs under 21st century sea-level rise. *Proceedings of the National Academy of Sciences* **111,** 3292–3297 (2014).

33. Craft, C. *et al.* Forecasting the effects of accelerated sea-level rise on tidal marsh ecosystem services. *Frontiers in Ecology and the Environment* **7,** 73–78 (2009).

34. IPCC. *Climate Change 2022: Impacts, Adaptation, and Vulnerability. Contribution of Working Group II to the Sixth Assessment Report of the Intergovernmental Panel on Climate Change* (eds Pörtner, H.-O. *et al.*) (Cambridge University Press, Cambridge, United Kingdom and New York, NY, USA, 2022).

35. Christian, J. E., Robel, A. A. & Catania, G. A probabilistic framework for quantifying the role of anthropogenic climate change in marine-terminating glacier retreats. *The Cryosphere,* 1–28 (2022).

36. Nias, I. J., Cornford, S. L., Edwards, T. L., Gourmelen, N. & Payne, A. J. Assessing uncertainty in the dynamical ice response to ocean warming in the Amundsen Sea Embayment, West Antarctica. *Geophysical Research Letters* **46,** 11253–11260 (2019).

37. Nias, I. J., Nowicki, S., Felikson, D. & Loomis, B. Modeling the Greenland Ice Sheet's Committed Contribution to Sea Level During the 21st Century. *Journal of Geophysical Research: Earth Surface* **128,** e2022JF006914 (2023).

38. Aschwanden, A. & Brinkerhoff, D. Calibrated Mass Loss Predictions for the Greenland Ice Sheet. *Geophysical Research Letters* **49,** e2022GL099058 (2022).

39. Ritz, C. *et al.* Potential sea-level rise from Antarctic ice-sheet instability constrained by observations. *Nature* **528,** 115–118 (2015).

40. Wernecke, A., Edwards, T. L., Nias, I. J., Holden, P. B. & Edwards, N. R. Spatial probabilistic calibration of a high-resolution Amundsen Sea Embayment ice sheet model with satellite altimeter data. *The Cryosphere* **14,** 1459–1474 (2020).

41. Asay-Davis, X. S., Jourdain, N. C. & Nakayama, Y. Developments in simulating and parameterizing interactions between the Southern Ocean and the Antarctic ice sheet. *Current Climate Change Reports* **3,** 316–329 (2017).

42. Bradley, A. T., Rosie Williams, C., Jenkins, A. & Arthern, R. Asymptotic analysis of subglacial plumes in stratified environments. *Proceedings of the Royal Society A* **478,** 20210846 (2022).

43. Bradley, A. T., De Rydt, J., Bett, D. T., Dutrieux, P. & Holland, P. R. The ice dynamic and melting response of Pine Island Ice Shelf to calving (2022).

44. Seroussi, H. *et al.* Continued retreat of Thwaites Glacier, West Antarctica, controlled by bed topography and ocean circulation. *Geophys. Res. Lett.* **44,** 6191–6199 (2017).

45. Snow, K. *et al.* The Response of Ice Sheets to Climate Variability. *Geophys. Res. Lett.* **44,** 11, 878–11, 885 (2017).

46. De Rydt, J. & Gudmundsson, G. H. Coupled ice shelf-ocean modeling and complex grounding line retreat from a seabed ridge. *J. Geophys. Res. Earth Surf.* **121,** 865–880 (2016).

47. Favier, L. *et al.* Assessment of sub-shelf melting parameterisations using the ocean–ice-sheet coupled model NEMO (v3. 6)–Elmer/Ice (v8. 3). *Geosci. Model Dev.* **12,** 2255–2283 (2019).

48. Webber, B. G. *et al.* Mechanisms driving variability in the ocean forcing of Pine Island Glacier. *Nature communications* **8,** 14507 (2017).

49. Dutrieux, P. *et al.* Strong sensitivity of Pine Island ice-shelf melting to climatic variability. *Science* **343,** 174–178 (2014).

50. Jourdain, N. C., Mathiot, P., Burgard, C., Caillet, J. & Kittel, C. Ice shelf basal melt rates in the Amundsen Sea at the end of the 21st century. *Geophysical Research Letters* **49,** e2022GL100629 (2022).

51. Burgard, C., Jourdain, N. C., Reese, R., Jenkins, A. & Mathiot, P. An assessment of basal melt parameterisations for Antarctic ice shelves. *The Cryosphere Discussions* **2022,** 1–56. `https://tc.copernicus.org/preprints/tc-2022-32/` (2022).

52. Lazeroms, W. M., Jenkins, A., Gudmundsson, G. H. & Van De Wal, R. S. Modelling present-day basal melt rates for Antarctic ice shelves using a parametrization of buoyant meltwater plumes. *The Cryosphere* **12,** 49–70 (2018).

53. Otto, F. E. Attribution of weather and climate events. *Annual Review of Environment and Resources* **42,** 627–646 (2017).

54. Vargo, L. J. *et al.* Anthropogenic warming forces extreme annual glacier mass loss. *Nature Climate Change* **10,** 856–861 (2020).

55. Roe, G. H., Christian, J. E. & Marzeion, B. On the attribution of industrial-era glacier mass loss to anthropogenic climate change. *The Cryosphere* **15,** 1889–1905 (2021).

56. Vaughan, D. G. & Arthern, R. Why is it hard to predict the future of ice sheets? *Science* **315,** 1503–1504 (2007).

57. Bamber, J. L., Oppenheimer, M., Kopp, R. E., Aspinall, W. P. & Cooke, R. M. Ice sheet contributions to future sea-level rise from structured expert judgment. *Proceedings of the National Academy of Sciences* **116,** 11195–11200 (2019).

58. Surawy-Stepney, T., Hogg, A. E., Cornford, S. L. & Davison, B. J. Episodic dynamic change linked to damage on the thwaites glacier ice tongue. *Nature Geoscience,* 1–7 (2023).

59. Liu, Y. *et al.* Ocean-driven thinning enhances iceberg calving and retreat of Antarctic ice shelves. *Proceedings of the National Academy of Sciences* **112,** 3263–3268 (2015).

60. DeConto, R. M. & Pollard, D. Contribution of Antarctica to past and future sea-level rise. *Nature* **531,** 591–597 (2016).

61. Aschwanden, A., Bartholomaus, T. C., Brinkerhoff, D. J. & Truffer, M. Brief communication: A roadmap towards credible projections of ice sheet contribution to sea level. *The Cryosphere* **15,** 5705–5715 (2021).

62. Robel, A. A., Seroussi, H. & Roe, G. H. Marine ice sheet instability amplifies and skews uncertainty in projections of future sea-level rise. *Proceedings of the National Academy of Sciences* **116,** 14887–14892 (2019).

63. Hawkins, E., Smith, R. S., Gregory, J. M. & Stainforth, D. A. Irreducible uncertainty in near-term climate projections. *Climate Dynamics* **46,** 3807–3819 (2016).

64. Stott, P. How climate change affects extreme weather events. *Science* **352,** 1517–1518 (2016).

65. Cornford, S. L. *et al.* Results of the third marine ice sheet model intercomparison project (MISMIP+). *The Cryosphere* **14,** 2283–2301 (2020).

66. Jaynes, E. T. *Probability theory: The logic of science* (Cambridge university press, 2003).

67. Arthern, R. J. Exploring the use of transformation group priors and the method of maximum relative entropy for Bayesian glaciological inversions. *Journal of Glaciology* **61,** 947–962 (2015).

68. Reese, R., Gudmundsson, G. H., Levermann, A. & Winkelmann, R. The far reach of ice-shelf thinning in Antarctica. *Nature Climate Change* **8,** 53–57 (2018).

69. Fürst, J. J. *et al.* The safety band of Antarctic ice shelves. *Nature Climate Change* **6,** 479–482 (2016).

70. Arthern, R. J. & Williams, C. R. The sensitivity of West Antarctica to the submarine melting feedback. *Geophysical Research Letters* **44,** 2352–2359 (2017).

71. De Rydt, J., Reese, R., Paolo, F. S. & Gudmundsson, G. H. Drivers of Pine Island Glacier speed-up between 1996 and 2016. *The Cryosphere* **15,** 113–132 (2021).

72. Medley, B. *et al.* Constraining the recent mass balance of Pine Island and Thwaites glaciers, West Antarctica, with airborne observations of snow accumulation. *The Cryosphere* **8,** 1375–1392 (2014).

73. Bradley, A. T., Arthern, R. J., Williams, C. R., Bett, D. T. & Byrne, J. *WAVI.jl: Ice sheet modelling in Julia*

74. Goldberg, D. N. A variationally derived, depth-integrated approximation to a higher-order glaciological flow model. *Journal of Glaciology* **57,** 157–170 (2011).

75. Holland, P. R., Jenkins, A. & Holland, D. M. The response of ice shelf basal melting to variations in ocean temperature. *J. Clim.* **21,** 2558–2572 (2008).

76. Jourdain, N. C. *et al.* A protocol for calculating basal melt rates in the ISMIP6 Antarctic ice sheet projections. *The Cryosphere* **14,** 3111–3134 (2020).

77. Marshall, J., Hill, C., Perelman, L. & Adcroft, A. Hydrostatic, quasi-hydrostatic, and nonhydrostatic ocean modeling. *Journal Geophys. Res. Oceans* **102,** 5733–5752 (1997).

78. McDougall, T. J., Jackett, D. R., Wright, D. G. & Feistel, R. Accurate and computationally efficient algorithms for potential temperature and density of seawater. *J. Atmos. Ocean. Technol.* **20,** 730–741 (2003).

79. Pacanowski, R. & Philander, S. Parameterization of vertical mixing in numerical models of tropical oceans. *J. Phys. Oceanogr.* **11,** 1443–1451 (1981).

80. Holland, D. M. & Jenkins, A. Modeling thermodynamic ice–ocean interactions at the base of an ice shelf. *J. Phys. Oceanogr.* **29,** 1787–1800 (1999).